

1

The feasibility of using distributed acoustic sensors in surface seismic application

2 **Samir F. Jreij, Whitney J. Trainor-Guitton, and James L. Simmons**

3 Colorado School of Mines,

4 1500 Illinois Ave,

5 Golden, CO, 80401

6 (May 3, 2018)

7 Running head: **The feasibility of using distributed acoustic sensors in surface seismic
application**

ABSTRACT

9 The PoroTomo survey at Brady's Natural Lab consisted of 238 multi-component geophones that
10 are spaced anywhere from 60 to 150 meters apart. This proves to be a difficult migration problem
11 with such sparse spacing. An imaging technique that utilizes both multi-component geophones
12 and a surface distributed acoustic sensor (DAS) acquisition attempts to resolve the spatial sampling
13 issue. Fortunately, the PoroTomo survey consisted of surface DAS cable with a 1-meter receiver
14 spacing along the fiber. Both 2D and 3D numerical experiments test the feasibility of using the
15 broadside sensitive multi-component geophones and the densely sampled DAS data together to
16 minimize insensitivity to certain waves. The objective of these experiments are to analyze if the
17 densely sampled DAS fiber data can help improve the image produced by the sparsely sampled
18 geophones. In 2D, a reflectivity model is created from the local fault model in the PoroTomo Survey.
19 Quantitative analysis provides an unbiased comparison of the results. The quantitative analysis
20 utilizes a convolutional neural network to prove that DAS adds value to imaging efforts. A more

21 challenging example in 3D confirms the conclusions made in 2D. A methodology to model DAS
22 data in 3D shows that utilizing DAS in surface surveys with sparse, multi-component geophones
23 proves to be useful in improving the classification accuracy of the image. The results, however,
24 are inconclusive because the migrated images are too low of a frequency to analyze due to the
25 limitation of the velocity model. Lessons learned from the data collected at the PoroTomo survey
26 and the numerical experiments are that a more regular acquisition geometry of the horizontal DAS
27 fiber increases identifying the true reflectors.

INTRODUCTION

28 Distributed acoustic sensing (DAS) is a technology that uses Rayleigh scattering in a fiber-optic
29 cable to detect elastic signals when wave particle motion is parallel to the sensing fiber (Hornman
30 et al., 2013). The two main components used in distributed sensing are the interrogator unit and the
31 fiber-optic cable. The interrogator unit works as a light source and receiver. It sends a known pulse
32 of light down the fiber. Nearly any type of existing fiber-optic cable can be used in conjunction
33 with an interrogator unit. Small imperfections within the fiber cause backscattering of light. Strain
34 events along the fiber cause this backscattering to change slightly when a wavefield approaches the
35 fiber. The interrogator unit can measure the Rayleigh backscattering and relate it to the strain along
36 the fiber.

37 **DAS Advantages**

38 DAS has many advantages in various industries. For one, DAS is a low-cost acquisition system
39 in wells that already contain fiber optic cables. Even in those wells that do not already contain
40 fiber optic cables, a DAS vertical seismic profile (VSP) is often more affordable than renting and
41 deploying geophones (Mateeva et al., 2014). DAS also enables seismic surveys to be acquired with
42 dense sampling (as small as 10-centimeter receiver spacing) at long cable lengths (tens of kilometers
43 long). Achieving even 1-meter sampling with conventional geophone is expensive and logically
44 difficult. Lastly, DAS has almost perfect repeatability in 4-D surveys when cemented in a borehole,
45 attached to casing, or trenched in the subsurface (Mateeva et al., 2013).

46 **DAS Disadvantages**

47 Although DAS may seem like the solution to seismic acquisition, it also has many disadvantages.
48 DAS is most sensitive to waves that have particle motion parallel to the orientation of the fiber, so
49 it is said that the technology has broadside insensitivity. Multi-component geophones also have this
50 issue; with more recording components, however, they are able to resolve more of the wavefield and
51 are not affected by this broadside insensitivity as much.

52 Another disadvantage is that DAS coupling is not trivial in all environments. In a borehole
53 environment, DAS can be cemented behind casing or permanently installed on production tubing
54 (Mateeva et al., 2013). Surface distributed sensor coupling is a more challenging issue. Lindsey
55 et al. (2017) describe how fibers can be utilized in loosely coupled environments. The Stanford
56 Fiber Optic Array consists of a 2.5 km long array that lies in a conduit about 1 to 2 meters below
57 ground. The DAS fiber geometry is restricted by the conduits, though, and the task of installing the
58 fiber is more difficult if there are no existing conduits. Daley et al. (2013) have trenched the cable
59 and returned at a later time to shoot the seismic survey. Although this method is effective, waiting
60 to shoot a survey at a later time can be inconvenient.

61 **Previous Work**

62 Historically, DAS has been used in a borehole environment for flow monitoring, temperature mea-
63 surements, and vertical seismic profiles (Clarke and Sandberg, 1983; Krohn et al., 2000; Mestayer
64 et al., 2011; Barberan et al., 2012; Cox et al., 2012; Daley et al., 2013; Mateeva et al., 2014).

65 Mestayer et al. (2011) describe how permanently installed fiber-optic infrastructure in existing
66 wells can enable low-cost non-intrusive geophysical monitoring. Geophones generally only acquire
67 data along a short subset of the well due to the limited number of receivers at predetermined receiver

spacing in VSP receiver arrays. This makes repeatable time-lapse surveys difficult as placing the geophones in the same location is not trivial. Mestayer et al. (2011) also discuss how borehole DAS is able to improve repeatability and time-lapse sensitivity because it is able to acquire data along the full well with a single shot. Mateeva et al. (2014) also describe a time lapse, 3D DAS VSP application. They conclude that DAS has many major business impacts on fields that require enhanced oil recovery (EOR) including cost efficiency, safety, and synergy with other fiber optic applications.

Barberan et al. (2012) discuss different ways DAS fiber can be coupled in a borehole environment. DAS fiber can be clamped to production tubing and used as a downhole seismic sensor. Barberan et al. (2012) expand on this explaining that acquiring seismic data over the entire well is essential for acquiring additional transit times for velocity inversion and it allows for a wide range of incidence angles in terms of wave directions that arrive at the fiber for inversion.

Daley et al. (2013) describes field tests from both horizontal and borehole distributed sensors. They conclude that the signal-to-noise (SNR) in surface DAS is not sufficient for observing P-waves and that DAS is more useful in borehole environments or longer surface arrays. They don't go into detail, however, regarding why certain waves are not observable in DAS.

As seen in these examples, DAS research has emphasized acquiring data in borehole environments because many wells are already equipped with fiber for production. As a result, acquiring DAS in boreholes is as simple as connecting the existing fiber-optic cable to a new interrogator unit that senses acoustic signal. Although there are some studies on surface DAS acquisitions (Daley et al., 2013; Hornman, 2017), there has not been a thorough study in active source experiments.

Daley et al. (2013) experiment with a vertical vibrator (vertical-force) source. The reflected P-wave is not recorded on the DAS fiber as the experiment only had 1,000 meters of offset, and,

91 therefore, the authors concluded that the SNR in surface DAS is insufficient for observing P-waves
92 due to the relatively small incidental reflected angle. Other source mechanisms must be investigated
93 before such a conclusion can be made about the feasibility of using surface DAS fiber. Another
94 option is utilizing the DAS fiber along with geophones to attempt to minimize the insensitivity of
95 some waves. This paper explores different imaging experiments using the field geometry from the
96 PoroTomo survey in Northwest Nevada and numerical modeling to explain how DAS fiber can help
97 minimize the insensitivity to waves in conjunction with geophones. The objective of these experi-
98 ments is to analyze if the densely sampled DAS fiber data can help improve the image produced by
99 the sparsely sampled geophones.

100 **PoroTomo Survey**

101 The PoroTomo survey involved four-weeks of data acquisition of geodesy, interferometric syn-
102 thetic aperture radar (InSAR), hydrology, temperature sensing, passive source seismology, and ac-
103 tive source seismology data (Feigl, 2017; Cardiff et al., 2018). The variety of data that were col-
104 lected at the PoroTomo survey lead to the origin of the experiments name: Poroelastic Tomography
105 by Adjoint Inverse Modeling of Data from Seismology, Geodesy, and Hydrology (or PoroTomo for
106 short). These data were jointly collected to characterize and monitor changes in the rock mechanical
107 properties of Brady's Natural Laboratory (BNL), an Enhanced Geothermal System (EGS) reservoir.

108 This paper investigates the active seismic source component of the PoroTomo Experiment. The
109 PoroTomo survey is one of the most unique seismic acquisitions for surface DAS fiber. The survey
110 included 238 multi-component geophones, 156 three-component (vertical and orthogonal horizon-
111 tal) vibroseis source locations that swept from 5 to 80 Hz in 20 seconds, 300 meters of borehole
112 DAS, and nearly nine kilometers of surface fiber-optic cable. The full survey geometry is shown in

113 Figure 1. As seen in Figure 1, the geophones are sparsely spaced with an average inline spacing of
114 80 meters. This paper focuses on identifying a methodology to resolve the spatial sampling issue.
115 The objective of this paper is to identify if the densely sampled DAS data can help improve the
116 image produced by the sparsely sampled geophones. Both 2D and 3D numerical experiments are
117 performed to test the feasibility of using the broadside sensitivity of multi-component geophones
118 and the dense sampling DAS data together to minimize insensitivity to certain waves.

FIBER SENSITIVITY

119 Understanding how DAS fiber works is essential to working with the data that are currently available
120 and to design effective future surveys. For a conventional DAS seismic survey, a known pulse of
121 light is sent into the fiber using an interrogator unit and some of the light is naturally scattered back
122 due to imperfections within the fiber. The interrogator unit is able to record this scattered light along
123 the fiber up to 10-kilometers away. This is known as the base condition inside of the fiber. The fiber
124 undergoes a strain when a seismic wavefield approaches and a scattering of light is produced that is
125 different from the base condition. The interrogator unit is able to relate this new scattering of light
126 to local strain along the fiber by recording the time of arrival and the phase-lag of the returning light
127 signals (Parker et al., 2014).

128 DAS fiber is most sensitive to waves that are able to stretch and squeeze the fiber, so the waves
129 have to have particle motion parallel to the orientation of the fiber. Every seismic sensor has its own
130 distinct sensitivity to the various types of waves depending on their emergent angle. The emergent
131 angle (θ) represents the angle between the incoming wave and the surface of the Earth. Consider a
132 plane wave reflection in the X-Z plane: an emergent angle of 0° represents a wave arriving parallel
133 to the surface (or a plane wave traveling in the Z-direction); an emergent angle of 90° represents a

134 wave arriving perpendicular to the surface (or a plane wave traveling in the X-direction).

135 These points can be demonstrated with a simple 2D example. Consider wave propagation in
136 the X-Z plane in a homogeneous, flat-layered, isotropic or vertical transverse isotropic medium
137 (Figure 2a-2b). The horizontal DAS fiber is oriented in the x-direction. P-waves have particle
138 motion parallel to the direction of wave propagation (Aki and Richards, 1980). Normal-incidence
139 reflections from a horizontal reflector will arrive perpendicular to the surface fiber. Data will not
140 be seen at short offsets in the case of a reflected P-wave (Figure 2a). The particle motion of P-
141 waves is parallel to the direction of propagation, so at short offsets, the reflected P-wave will arrive
142 perpendicular to the fiber. As seen in Figure 3a, P-waves with a 0° emergent angle show zero
143 amplitude on the fiber and maximum amplitude on the z-component of a geophone, following a
144 $\cos^2(\theta)$ decay with emergent angle (θ). Moving to further offsets yields emergent angles that are
145 at a larger angle to the fiber. According to Figure 3a, these waves will show more data than waves
146 arrive perpendicular to the fiber as they are propagating in the direction of the fiber and will show
147 less data on the vertical component of the geophone. The further the offset, however, the lower the
148 amplitude of the wave due to attenuation effects.

149 Shear-waves are potentially more interesting when recording with horizontal fiber. Consider
150 again 2D wave propagation in the X-Z plane in a homogeneous, flat-layered, isotropic or vertical
151 transverse isotropy medium (Figure 2b). SV-waves have particle motion in the X-Z plane, as do
152 P-waves (Aki and Richards, 1980). Normal-incidence reflections from a horizontal reflector will
153 arrive perpendicular to the surface fiber. P-wave particle motion, as stated previously, will be in the
154 z direction, and consequently, will not be recorded by the fiber. SV wave particle motion will be
155 in the x-direction (emergent angle of 0°), and the DAS response will be maximum (Figure 3b). At
156 larger offsets, the SV-wave emerging angle begins to approach 90° . A larger emerging angle means
157 less signal (Figure 3b) is recorded by both the surface DAS and the x-component of the geophone

158 because the SV-wave particle motion is in the vertical perpendicular to the fiber (Figure 2b).

159 We also consider using SH-waves with the same 2D survey geometry (homogeneous, flat-
160 layered, isotropic). S-H waves have particle motion perpendicular to the direction of wave propa-
161 gation or, in this case, in the y-direction. The DAS response to SH-waves will be zero since the SH
162 particle motion is perpendicular to the DAS fiber, in the y-direction. In this 2D case, the SH-wave
163 will be out of plane regardless of source-receiver offset. In 3D, SH-waves can be seen on the DAS
164 if they are properly oriented. For example, a source-receiver azimuth perpendicular to the 2D fiber
165 (in this case, in the y-direction) will produce a maximum amplitude reflection on the DAS since
166 the particle motion is in the x-direction for all offsets. As the source-receiver azimuth moves inline
167 with the fiber, the SH-wave particle motion decreases, and is equal to zero when the source-receiver
168 azimuth is inline with the fiber.

169 In this section, DAS fiber directionality was described analytically and depicted graphically.
170 The directionality is important to understand when creating a seismic survey geometry to assist
171 with geophone deficiencies.

2D NUMERICAL MODELING EXAMPLES

172 Imaging the geophone data is a difficult task in the PoroTomo Survey due to the irregular spatial
173 sampling and offset. This paper focuses on identifying a way to resolve the spatial sampling issue.
174 Fortunately, the PoroTomo survey includes surface DAS cable that has 10-meter gauge-length and
175 an equivalent of 1-meter receiver spacing along the fiber. Many papers in the literature are interested
176 in methods to convert DAS measurements (strain or strain rate) to a geophone equivalent (particle
177 velocity or displacement) with the intent to replace point sensors with distributed sensors, or use
178 existing geophone processing to clean up DAS data (Daley et al., 2013, 2015; Jreij et al., 2017).

179 The idea of using both data types in simultaneous imaging is explored in this paper to produce more
180 detailed images using synthetic examples.

181 **2D Synthetic Design**

182 Siler and Faulds (2013) mapped the faults of Brady's Natural Lab shown in Figure 4. It is important
183 to image these faults in detail as they are driving factors behind the recharge of the geothermal
184 reservoir (Feigl, 2017; Folsom et al., 2018). A slice is taken from the Brady's Natural Lab fault
185 model (Siler and Faulds, 2013) in the PoroTomo Survey and used as a reflection velocity models.
186 This slice is shown in Figure 5. The Siler and Faulds (2013) fault model slice is used as a reflectivity
187 model as it contains a variety of structural dips.

188 Seismic sources in the PoroTomo experiment are not on a uniform grid. In fact, the source
189 spacing is as large as 150 meters. Seismic illumination describes how much of the subsurface can
190 be imaged given a source-receiver geometry and velocity model. Illumination in seismic surveys
191 is highly influenced by source-receiver spacing. For the purpose of this section, a constant source
192 spacing of 75 meters (which is about the average source spacing in the PoroTomo survey) is used
193 to minimize migration artifact effects from poor illumination. For the 2D experiments present in
194 this paper, both vertical and horizontal force sources are modeled to represent a vertically and a
195 horizontal vibe, respectively, which were also collected at BNL for the PoroTomo field experiment.

196 Reverse time migration (RTM) is the imaging technique that is used for the experiments in this
197 paper. 2D elastic forward modeling is used to produce strain (as measured by DAS) and displace-
198 ment (as measured by geophones) data along the surface of our 2D example excited by a vertical
199 force source. Receivers at every one meter across the experiment are used for recording. As seen
200 in Figure 1, the PoroTomo survey did not include a straight fiber that was this long. It did include,

201 however, a maximum offset of 1,500-meters across the entire survey. A 2D line of 1,500 meters was
202 utilized to gather data with similar offsets as the PoroTomo survey.

203 The code generated for these experiments outputs both strain and displacement at every receiver
204 location. The average geophone spacing is about 70 meters in the PoroTomo experiment. A geo-
205 phone spacing of 100 meters is chosen to analyze geophone spacing closer to the extremes of this
206 experiment. The recorded data are generated from a reflectivity model that is derived from Brady's
207 fault model using an elastic finite difference modeling (FDM) operator from the Madagascar pack-
208 age (Fomel et al., 2013). The next step is to back propagate the recorded data from this forward
209 modeling to recover the receiver wavefield. If this was a field experiment, the field data would be
210 back propagated. Two different sources are needed to create the receiver wavefield. An acceleration
211 force is used for back propagation of the geophone data and a stress tensor is used for back propaga-
212 tion of the DAS data. The proper way to do imaging is to back propagate the two data types (strain
213 and displacement) simultaneously, but this was not possible with current codes, so the data are back
214 propagated individually.

215 The last wavefield that needs to be generated is the source wavefield. The source wavefield is a
216 forward model from the original source location through a smooth velocity model. It is important
217 that the velocity model is smooth as reflections will cause an improper final image. Now, a source
218 and two receiver wavefields exist. An imaging condition is required to combine the wavefields.

219 Traditionally, the zero-lag, cross correlation imaging condition (IC) is used to create a migrated
220 image (Claerbout, 1985). Although this methodology may provide a solution for elastic imaging,
221 this IC produces four resulting images (PP, PS, SP, SS). This proves to be a more difficult compari-
222 son between different data types for the purpose of this paper. Rocha et al. (2016) describes the use
223 of an energy-norm based IC that exploits wavefield directionality to create a single elastic image

224 that represents the measure of reflected energy. There are many other benefits to using the energy-
225 norm IC, but most important for this work is that one final image allows for an easy comparison of
226 migrated elastic data.

227 The image produced from the elastic energy norm RTM with sparsely sampled multi-component
228 geophones using a vertical force is shown in Figure 6a. This image shows reflectors are discontin-
229 uous and difficult to follow. The image is also covered with migration artifacts due to insufficient
230 sampling of the wavefield. An example of this is presented around 800 meters on the x-axis of
231 Figure 6a: the migration artifacts make it difficult for an interpreter to follow the shallow reflector.
232 The deeper reflector in Figure 6a is impossible to identify.

233 The image produced from the elastic energy norm RTM with DAS fiber along the surface of the
234 model creating a virtual receiver at every one meter is shown in Figure 6b. The shallow reflector in
235 this image is sharp and continuous, allowing for easy interpretation. Although migration artifacts
236 are still present around 800 meters on the x-axis, these are different from those experienced in
237 Figure 6a. These migration artifacts are now due to fake modes present because the wavefield is
238 extrapolated using only the x-component data that was recorded with DAS fiber.

239 Now there are two images with two different migration artifacts (i.e. types of noise). Stacking
240 the images should theoretically reduce the noise and highlight the reflection events. Linearly stack-
241 ing the events, however, will not currently work as the amplitudes are on different scales. Instead,
242 the amplitudes of both images are normalized by the maximum and then stacked to produce Fig-
243 ure 6c. Although Figure 6c still has artifacts in it, the reflectors are enhanced and the image is easier
244 to interpret than Figure 6a or Figure 6b.

245 Fiber attributes were discussed earlier in this paper. Different source types can generate different
246 polarizations of reflection events. For this reason, the second 2D experiment uses the same geometry

247 and model as the first experiment, but now an horizontal force is used to generate data. The image
248 produced from elastic energy norm RTM with sparsely sampled multi-component geophones and
249 a horizontal force is shown in Figure 7a. This image still shows some discontinuity in reflectors,
250 but the reflector is much easier to follow. The receiver sampling was not changed, so the image is
251 still covered with migration artifacts due to insufficient sampling of the wavefield. On the left-hand
252 side of the geophone image, the end of the dipping fault is not properly imaged. This is due to
253 insufficient aperture in the migration. The deeper reflector is now easier to identify in Figure 7a.

254 The image produced from elastic energy norm RTM with DAS data and an S-source is shown
255 in Figure 7b. The DAS image is still very sharp, but now the migration artifacts have diminished.
256 The deeper reflector is much easier to observe and interpret as well. This image is sharp because the
257 zero-offset SV-wave reflections are perfectly polarized to show the reflectors on DAS and the DAS
258 data is really well sampled.

259 There are two images with two different migration artifacts (i.e. types of noise), so the images
260 are normalized and stacked just as it was done for the previous example. The results are shown in
261 Figure 7c. Figure 7c shows both reflectors clearer than Figure 6c which suggests that a horizontal
262 force is more beneficial for near-offset DAS surveys.

263 **Value of Information**

264 All of the experiments presented in the paper can be qualitatively analyzed and discussed, but qual-
265 itative analysis is always different between people due to different biases and perspectives. A method
266 to quantitatively analyze the experiments is needed to do effective comparisons.

267 The Value of Information (VOI) is a quantitative tool that originates from the field of decision
268 analysis to quantify how relevant and reliable an information source is (Trainor-Guitton et al., 2013).

269 VOI estimates the possible increase in expected utility by gathering information. It is calculated by
 270 comparing the prior value (V_{prior} , the average utility of a decision made with current information)
 271 to the value with imperfect information ($V_{imperfect}$) by subtracting the two, shown in Equation 1.

$$VOI = V_{imperfect} - V_{prior} \quad (1)$$

272 The goal of this project is to observe if there is any added value to using distributed acoustic
 273 sensing in surface acquisitions. The value with imperfect information shown in Equation 2 can only
 274 be calculated with a quantitative measure of how accurate the information source as,

$$V_{imperfect} = \sum_{j=F,NF} Pr(\theta^{int} = \theta_j) \max_a [\sum_{i=F,NF} Pr(\theta = \theta_i | \theta^{int} = \theta_j) v_a(\theta_i)] \quad (2)$$

275 This quantitative measure can be represented by the posterior probability, $Pr(\theta = \theta_i | \theta^{int} = \theta_j)$,
 276 within the value with imperfect information (Equation 2). Specifically for these problems, the
 277 posterior probability can be how often interpretations of faults align with the actual presence of
 278 faults. It is important to calculate the posterior reliability so the value of imperfect information can
 279 be completed. The posterior probability can be calculated using Equation 3,

$$Pr(\theta = \theta_i | \theta^{int} = \theta_j) = \frac{(Pr(\theta = \theta_i)) Pr(\theta^{int} = \theta_j | \theta = \theta_i)}{Pr(\theta^{int} = \theta_i)}; \forall i, j = F, NF \quad (3)$$

280 where θ represents a true value of Fault or Not Fault, θ^{int} represents an interpreted Fault or Not
 281 Fault. There are a variety of methodologies to produce information about whether an interpreted
 282 fault is actually a fault or not. This paper utilizes a machine learning approach to interpret the
 283 features in the migrated image.

284 **Convolutional Neural Network Analysis**

285 Machine learning is a field within computer science that focuses on the ability of computer systems
286 to learn patterns within data without being explicitly programmed for these patterns (Samuel, 1959).
287 Machine learning has had a large boom in the geophysics industry within the last 10 years.

288 There are a variety of machine learning algorithms that can be utilized based on the problem that
289 needs to be solved. One of the most powerful machine learning algorithms is the neural network.
290 Neural networks are inspired by the biological neural networks that constitute human brains or at
291 least how humans perceive they work (Gerven and Bohte, 2018). They consist of many layers in
292 parallel and every layer consists of a number of nodes. All neural networks consist of at least two
293 layers: the input layer and output layer. All the extra layers in between the input and output layers
294 are the hidden layers. The nodes of every layer are like neurons in the brain. Every neuron has its
295 own activation function that determines whether it should be “fired” or not similar to how a neuron
296 in the brain behaves. Each layer receives the output from the previous layer based on if the previous
297 neuron is fired or not.

298 Convolutional Neural Networks (CNN) in particular are at the core of most state-of-the-art com-
299 puter vision solutions for a wide variety of tasks. One of the most accurate CNN image classifiers
300 is the Inception-v3 model (Szegedy et al., 2015). The original Inception-v3 model is trained and
301 tested on the 2012 ImageNet Large Scale Visual Recognition Challenge (Russakovsky et al., 2015).
302 The training dataset consisted of 10,000,000 labeled images that depicted 1,000 object categories.
303 The Inception-v3 model was able to perform with 3.5% top-5 error, meaning that the target label
304 is within the top-5 probability classifications that the algorithm produced. A top-5 error of 3.5%
305 means the Inception-v3 model is able to perform with high accuracy, making it a top contender for
306 a geophysics image classification problem.

307 The Inception-v3 model utilizes transfer learning which means it stores knowledge gained from
308 training on the ImageNet dataset and then applies it to a different but related problem. It is difficult to
309 train a CNN from scratch because a large dataset is needed with a substantial amount of computers
310 equipped with GPU's. Instead, the intermediate layers of the Inception-v3 model are used as they
311 are already trained on detecting edges, shapes, and other high level features. The weights of the
312 model's last layer are recreated to identify if an image is either a fault or not a fault.

313 The Inception v3 model's ability to identify features can be leveraged within the geophysics
314 realm. The first step is to create some training data to retrain the model. The objective is to see
315 if DAS helped identify more faults than a sparse array of multi-component geophones. For the
316 experiments in this chapter, RTM images are created from 2D reflectivity slices of the Siler and
317 Faulds (2013) fault model. There are about 500 other slices along both the X and Y axis of the
318 PoroTomo grid. A number of these slices can be migrated to create training data for identifying
319 faults.

320 The next step is to take spatial windows of the migrated images and label them based on if there
321 are faults or not within the image. 100 meter by 100 meter (10 grid cell by 10 grid cell) subsets of
322 the migrated images were created. There are a large amount of data present and individually picking
323 whether an image contains a fault or not would be time consuming. As stated earlier, the true fault
324 model exists to compare with the migrated images. The same subset of the migrated images can
325 be compared with the reflectivity model. If more than half the pixels are a fault, then the program
326 labels the training data as a fault (Figure 8a). Otherwise, the program labels the training data as not
327 a fault (Figure 8b).

328 This is an easy and automatic way to generate training data, but training is an essential step
329 prior to testing, so it needs to be continually improved. The next step is to QC the training data to

330 make sure that the examples are actually of “faults” and “not faults”. Many iterations are required
331 until an acceptable cross-validation accuracy is achieved. A total of 2500, 100 meter by 100 meter
332 windowed RTM images were used to train the CNN to detect faults. A final training validation
333 accuracy of 94.4% is achieved. This is an acceptable accuracy check and now the neural network is
334 ready to be tested on data that were not included in the training data.

335 A 100 meter by 100 meter testing data is created the same way the training data is created. The
336 testing data is kept hidden from the training data. The first RTM image that is used for testing is
337 the vertical source data from the velocity model shown in Figure 5. The first test is on the sparse,
338 multi-component geophone image (Figure 6a). The RTM image is decomposed into 3,625 (100
339 meter x 100 meter) images with labels of “Faults” and “Not Faults”. This same process is used for
340 the synthetic created from DAS and multi-component geophones.

341 A posterior reliability of information can be calculated with the results from the testing data.
342 The resulting posterior reliability of information is shown graphically in Figure 9a and Figure 9b
343 for a vertical force and a horizontal force, respectively.

344 The results from Figure 9a for the vertical source show that adding DAS into the sparse array
345 of geophones with Figure 5 as the velocity model improves the classification of faults by 20%.
346 However, there is an increase in false negatives by about 30%. This means either the normalized,
347 stacked image has many artifacts or the classifier needs to be better trained on what is not a fault.
348 The number of false positives decreases by 20% which is a substantial amount. Lastly, the number
349 of true negatives decreases by almost 30%. This confirms that the classifier needs to be better trained
350 on what is not a fault.

351 The results from Figure 9b for the horizontal source show that adding DAS into the sparse array
352 of geophones with Figure 5 as the velocity model decreases the classification of faults by about 1%.

353 However, the classification of true negatives increases by about 5% and false negatives decreases by
354 about 5% meaning the DAS data did add some value to the CNN classification.

355 **2D Summary**

356 This section discussed in great detail how 2D DAS data can be modeled. It also showed how a
357 long offset, 2D surface DAS line can produce a sharp resulting image. A quantitative analysis using
358 a machine learning methodology showed that DAS does add value to sparse geophone arrays. A
359 quantitative analysis also shows that using a horizontal force with DAS allows for sharper images.
360 These hypotheses must now be confirmed with a 3D acquisition.

3D NUMERICAL MODELING EXAMPLES

361 The objective of this paper is to observe if there is any added value of using surface DAS with
362 sparsely sampled, multi-component geophones. In the previous section, we observed that in a long
363 2D line, there is added value using DAS to help with the spatial sampling. In 3D, however, there
364 are many more complications than in 2D. This section explores additional examples of using DAS
365 in combination with multi-component geophones, but now with the PoroTomo 3D survey geometry.
366 These examples utilize numerical modeling to understand more about what is recorded.

367 A velocity model from sweep interferometry shown in Figure 10 was used to create data (Matzel
368 et al., 2017a). As in the previous section, a modified version of the conventional elastic FDM code
369 (ewefdm) present in Madagascar (Fomel et al., 2013) is utilized, but now for the 3D case. This
370 allows us to recover both displacement and strain data along receivers in the grid. A variable density
371 is now used to create reflectivity instead of using purely velocity changes to create reflectivity in the
372 2D case.

373 **3D Modeling of Non-Uniform DAS Acquisition**

374 The wavefield along the fiber is now recorded for the six components of strain (XX, XY, XZ, YY,
 375 YZ, and ZZ). Field DAS data with single fiber, however, does not recover all six components. In-
 376 stead, it only recovers contributions of the wavefield in the direction that it is oriented. We can
 377 project the six components from the synthetic data on to the vector direction of the field fiber loca-
 378 tions to recover the strain in the direction that the fiber is oriented by using Equation 4,

$$\begin{bmatrix} \varepsilon_{ZZ} \\ \varepsilon_{XX} \\ \varepsilon_{YY} \\ \varepsilon_{XY} \\ \varepsilon_{YZ} \\ \varepsilon_{ZX} \end{bmatrix} = \begin{bmatrix} V_Z^2 & V_X^2 & V_Y^2 & 2V_XV_Y & 2V_YV_Z & 2V_ZV_X \end{bmatrix} = \begin{bmatrix} \varepsilon' \end{bmatrix} \quad (4)$$

379 where ε_{ij} is the strain in the direction ij , V_i is the vector projection in the i direction, and ε' is
 380 the strain in the direction of the fiber.

381 A matrix of fiber vector directions must be created prior to using Equation 4. The fiber endpoints
 382 were recorded in the field using a handheld GPS device after the fiber was trenched. The virtual
 383 receiver locations along the fiber were then interpolated at 1-meter spacing between these endpoints.
 384 Although this gives a good estimate of the x and y coordinates of the fiber, this does not give any
 385 information on how deep the fiber was trenched. For this reason, we assume that the fiber was
 386 all trenched in the same horizontal plane and there are no dips along the fiber. This simplifies
 387 Equation 4 to only have contributions from X and Y.

388 Applying Equation 4 recovers only one value of strain along the fiber. In reality, there are

389 contributions from both X and Y, so the strain matrix should have values at XX, YY, and XY. We
 390 can use the adjoint operation to recover a vector projection of the strain value from Equation 4. The
 391 adjoint operation shown in Equation 5 returns back to the original PoroTomo coordinate system.

$$\begin{bmatrix} \varepsilon' \end{bmatrix} = \begin{bmatrix} V_Z^2 \\ V_X^2 \\ V_Y^2 \\ 2V_X V_Y \\ 2V_Y V_Z \\ 2V_Z V_X \end{bmatrix} = \begin{bmatrix} \varepsilon_{ZZ} \\ \varepsilon_{XX} \\ \varepsilon_{YY} \\ \varepsilon_{XY} \\ \varepsilon_{YZ} \\ \varepsilon_{ZX} \end{bmatrix} \quad (5)$$

392 The last attribute of fiber that needs to be modeled is the gauge-length. As discussed earlier
 393 in this paper, the gauge-length of fiber is related to the wavelength recorded along the fiber and it
 394 acts as a moving average. The gauge-length in the PoroTomo survey was set at 10-meters, so the
 395 modeled data, d , is a matrix multiplication of $\frac{1}{10}$ for the gauge length, the spatial sampling 1-meter,
 396 and the raw point data, b , recorded by the finite difference code (shown in Equation 6, after Lim
 397 Chen Ning and Sava, 2018).

$$\begin{bmatrix} d_5 \\ d_6 \\ d_7 \\ \vdots \\ d_{n-5} \end{bmatrix} = \frac{1}{10} \begin{bmatrix} 1 & 1 & 1 & 1 & 1 & 1 & 1 & 1 & 1 & 1 & 0 & 0 & 0 & 0 \\ 0 & 1 & 1 & 1 & 1 & 1 & 1 & 1 & 1 & 1 & 1 & 0 & 0 & 0 \\ 0 & 0 & 1 & 1 & 1 & 1 & 1 & 1 & 1 & 1 & 1 & 0 & 0 & 0 \\ 0 & 0 & 0 & \ddots & 0 \\ 0 & 0 & 0 & 0 & 1 & 1 & 1 & 1 & 1 & 1 & 1 & 1 & 1 & 1 \end{bmatrix} \begin{bmatrix} b_5 \\ b_6 \\ b_7 \\ \vdots \\ b_{n-5} \end{bmatrix} \quad (6)$$

398 **Numerical Modeling**

399 It is important to image the faults in detail at Brady's Natural Lab as they are the driving factors
400 behind the recharge of the geothermal reservoir. Although Siler and Faulds (2013) would be a good
401 candidate for data modeling, a simpler model is needed to first test the hypothesis of imaging using
402 the two data types simultaneously. A four layer model with a variety of structures is used as the
403 density model for the first example (Figure 11). There is a contrast of about 300 g/cc between each
404 layer to ensure strong reflections.

405 The synthetic images are produced using the same methodology presented in the 2D section.
406 The results from migrating the DAS data are shown in Figure 12. The results from migrating the
407 geophone data are shown in Figure 13. A visual reflectivity model shown on the left of both figures
408 was produced by applying the Laplacian operator on Figure 11 and setting all values to one.

409 At first glance, it seems as if the DAS image does not have any reflectors. It can be compared
410 to the true reflectivity model shown on the right of Figure 12 to identify the signal in the image. It
411 is clear that the data recorded by the DAS fiber is too low in frequency to resolve the beds within
412 the image. This is due to both the velocity field that the experiment used to mimic the PoroTomo
413 subsurface and the FDM accuracy condition presented in Equation 7.

$$\frac{v_{min}}{f_{max}} > N * \sqrt{dx^2 + dy^2 + dz^2} \quad (7)$$

414 The minimum velocity of approximately 950 m/s from the input velocity field forces the maxi-
415 mum frequency of the wavelet to be 16 Hz and the peak frequency of the wavelet to be 12 Hz. This
416 equates to a 12 Hz wavelet and the velocity model corresponds to a wavelength of about 108 meters.

417 The DAS image (Figure 12) is also contaminated by fake modes and migration artifacts (Rocha

418 et al., 2016). Fake modes are expected since the displacement field is incomplete when wavefield
419 extrapolation was performed as the fiber is only recording one component of strain in the direction
420 that it is oriented. An inexperienced interpreter would eagerly interpret the fake modes as an area
421 of interest for further exploration methods.

422 At first glance, the geophone data also appear to have no clear reflection events. The image can
423 again be compared to the true reflectivity model overlain on the left of Figure 13 to identify the
424 signal in the image. The geophone image is also limited by the source wavelet that was injected
425 into the model. Differentiation between the thin beds is not possible using the source wavelet in this
426 experiment.

427 The geophone image, similar to the DAS image, is also contaminated by migration artifacts.
428 These migration artifacts, however, are due to the insufficient sampling that creates migration ar-
429 tifacts on the edge of reflectors. The wavefield is not sampled completely because the geophones
430 adopted from the PoroTomo survey are placed sparsely around the model (the average geophone
431 spacing is about 80 meters).

432 Quantitative Image Comparison

433 In 2D, a machine learning methodology was used to create a quantitative image comparison. Al-
434 though 3D CNN's exist, they are not as polished and readily available as are 2D CNN's. Instead, the
435 data are quantitatively analyzed using energy norm image filtering. Energy norm filtering focuses
436 on highlighting areas with reflected energy is maximum, so filtering the image based on an applied
437 limit will highlight where reflections may be coming from as opposed to migration artifacts. The
438 geophone and DAS images are combined by first normalizing the data types based on their maxi-
439 mum amplitude. They are then stacked together to test this hypothesis. This image would ideally

Table 1: Confusion matrix for top 90% energy reflected.

Top 90% energy reflected		
	θ_R^{int}	θ_{NR}^{int}
θ_R	184800	1206000
θ_{NR}	346700	1824000

440 highlight continuous reflectors with the densely sampled DAS data and reduce migration artifacts
 441 by extrapolating the full displacement wavefield with the multi-component geophones.

442 Every model cell that is above an applied limit is assigned a value of 1 and every model box that
 443 is below the limit is assigned a value of 0. A cell-by-cell comparison between the filtered, multi-
 444 component geophone image and the original reflectivity model is performed to identify how much
 445 additional accuracy is gained by adding the DAS data. The results of this cell-by-cell comparison
 446 are presented in confusion matrix form (Table 1), where R represents reflections and NR represents
 447 not reflections.

448 The confusion matrices assist in calculating the posterior value using Equation 3. The posterior
 449 value explains the probability that an event which the data type predicted is the event present. The
 450 posterior can then be used to calculate the utility or value of information added when using DAS
 451 and geophone versus only geophone with Equation 1. The results for the medium filter, posterior
 452 values in the four layer model presented in this paper are displayed in Figure 14.

453 In this experiment, adding distributed sensors increases the probability of finding if a cell is not
 454 a reflector and decreases the probability of false negatives. Adding distributed sensors, however,
 455 increases the probability of identifying false positives and decreases the probability of finding true
 456 reflectors. This experiment, however, is inconclusive in identifying if DAS has added value with
 457 sparsely sampled geophone data. A better DAS geometry must be tested to make further conclusions

458 on the effectiveness of surface DAS fiber.

459 The geometry shown in Figure 15 is utilized to further test the effectiveness of surface DAS
460 fiber. This new acquisition utilizes 25% less fiber and 60% fewer sources than the PoroTomo survey
461 geometry. Quantitative analysis using the energy norm filtering methodology is utilized again to
462 identify how well the survey imaged. The results are presented in Figure 16

463 Figure 16 shows a significant increase in true positives and decrease in false negatives. Al-
464 though there was an increase in false positives and a decrease in true negatives, the increase in true
465 positives proves that this new acquisition is better suited to image the subsurface with surface DAS
466 fibers. Energy norm imaging again allowed for an automatic method to interpret images output
467 from the migration images. Filtering images based on amplitudes is a crude approximation of how
468 an interpreter would “interpret” an image.

469 **3D Summary**

470 This section discussed differences in modeling DAS data in 3D versus 2D. The experiments in this
471 section helped clarify what kinds of data that a single surface DAS fiber can record. The experiments
472 discovered that the DAS configuration in the PoroTomo survey combined with the low frequency
473 nature of the modeling did not add value to the multi-component geophone imaging effort. Addi-
474 tionally, the percentages of missing strain components in 3D is larger than the 2D case, contributing
475 to the poor image quality. A better geometry and multi-component DAS were required to make
476 further conclusions on the effectiveness of DAS fiber in surface acquisition. Another experiment
477 was preformed with DAS fibers arranged in 2D lines. This acquisition geometry led to an increased
478 percentage of reflectors identified. It is concluded that the 2D surface DAS fiber lines are a better
479 suited geometry to image the subsurface.

CONCLUSIONS

480 In this paper, we discussed some of the fiber attributes that are essential to understand before looking
481 at surface DAS data. The most important attribute is the types of waves that fiber is directionally
482 sensitive. It is concluded that surface DAS in a flat-layered Earth model is sensitive to long offset
483 P-waves, short offset SV-waves, and SH-waves produced by a source that is perpendicular to the
484 fiber orientation.

485 It was discovered that the geophone data in the PoroTomo survey was too sparsely sampled, and
486 the hypothesis that densely sampled DAS data can fill in the gaps of the geophones was introduced.
487 This hypothesis was tested in 2D using elastic numerical modeling and RTM. It is then shown how
488 data are modeled for DAS receivers in 2D. The energy norm imaging condition was chosen as it
489 allowed for an easier method to compare two images than the conventional imaging condition. The
490 experiments showed that an inline horizontal force allows for the best results qualitatively due to the
491 resulting SV reflections. Lastly, this section explains the need for statistical and quantitative analysis
492 in the geophysics realm. A description of how to perform quantitative analysis using machine
493 learning methodology is presented. Both methods concluded that DAS added imaging value to
494 sparsely sampled multi-component geophones.

495 The 2D scenario did not test the full DAS fiber directionality. We discuss 3D numerical mod-
496 eling and RTM used to combine DAS and multi-component geophone data. The challenges of
497 modeling DAS in 3D are also discussed including recording the proper component of strain along
498 the fiber. The resulting migrated images did not clarify if DAS added any qualitative value to multi-
499 component geophone images as the migrated images were too low of a frequency to analyze due
500 to the limitation of the velocity model. A quantitative analysis of the combined image is utilized.
501 This chapter concluded that adding DAS data only helped to reduce the number of false positives

502 by a very small fraction. This experiment is inconclusive in regards to identifying if DAS can add
503 value to sparsely sampled geophone data, so another experiment was performed with 2D surface
504 DAS fiber lines. The new proposed experiment with long-offset, 2D surface fiber lines concluded
505 that using the new geometry was better suited for surface DAS acquisitions. The next proposed step
506 is to test this hypothesis with field data.

REFERENCES

- 507 Aki, K., and P. G. Richards, 1980, Quantative seismology: Theory and methods: New York, **801**.
- 508 Barberan, C., C. Allanic, D. Avila, J. Hy-Billiot, A. Hartog, B. Frignet, and G. Lees, 2012, Multi-
- 509 offset seismic acquisition using optical fiber behind tubing: Presented at the 74th EAGE Confer-
- 510 ence and Exhibition incorporating EUROPEC 2012.
- 511 Cardiff, M., D. D. Lim, J. R. Patterson, J. Akerley, P. Spielman, J. Lopeman, P. Walsh, A. Singh, W.
- 512 Foxall, H. F. Wang, et al., 2018, Geothermal production and reduced seismicity: Correlation and
- 513 proposed mechanism: Earth and Planetary Science Letters, **482**, 470–477.
- 514 Claerbout, J. F., 1985, Imaging the earth's interior: Blackwell scientific publications Oxford, **1**.
- 515 Clarke, R., and C. L. Sandberg, 1983, Fiber optic temperature sensing. (US Patent 4,417,782).
- 516 Cox, B., P. Wills, D. Kiyashchenko, J. Mestayer, J. Lopez, S. Bourne, R. Lupton, G. Solano, N.
- 517 Henderson, D. Hill, et al., 2012, Distributed acoustic sensing for geophysical measurement, mon-
- 518 itoring and verification: **37**, 7–13.
- 519 Daley, T., D. Miller, K. Dodds, P. Cook, and B. Freifeld, 2015, Field testing of modular borehole
- 520 monitoring with simultaneous distributed acoustic sensing and geophone vertical seismic profiles
- 521 at citronelle, alabama: Geophysical Prospecting.
- 522 Daley, T. M., B. M. Freifeld, J. Ajo-Franklin, S. Dou, R. Pevzner, V. Shulakova, S. Kashikar, D. E.
- 523 Miller, J. Goetz, J. Henninges, et al., 2013, Field testing of fiber-optic distributed acoustic sensing
- 524 (das) for subsurface seismic monitoring: The Leading Edge, **32**, 699–706.
- 525 Feigl, K. L., 2017, Overview and preliminary results from the porotomo project at brady hot springs,
- 526 nevada: Poroelastic tomography by adjoint inverse modeling of data from seismology, geodesy,
- 527 and hydrology: Presented at the Stanford Geothermal Workshop.
- 528 Folsom, M., J. Lopeman, D. Perkin, and M. Sophy, 2018, Imaging shallow outflow alteration to
- 529 locate productive faults in ormats bradys and desert peak fields using csamt.

- 530 Fomel, S., P. Sava, I. Vlad, Y. Liu, and V. Bashkardin, 2013, Madagascar: Open-source software
531 project for multidimensional data analysis and reproducible computational experiments: Journal
532 of Open Research Software, **1**.
- 533 Gerven, M. V., and S. Bohte, 2018, Artificial Neural Networks as Models of Neural Information
534 Processing.
- 535 Hornman, J., 2017, Field trial of seismic recording using distributed acoustic sensing with broadside
536 sensitive fibre-optic cables: Geophysical Prospecting, **65**, 35–46.
- 537 Hornman, K., B. Kuvshinov, P. Zwartjes, and A. Franzen, 2013, Field trial of a broadside-sensitive
538 distributed acoustic sensing cable for surface seismic: Presented at the 75th EAGE Conference
539 & Exhibition incorporating SPE EUROPEC 2013.
- 540 Jreij, S., W. Trainor-Guitton, D. Miller, et al., 2017, Field data comparison of 3d horizontal dis-
541 tributed acoustic sensing and geophones: SEG Technical Program Expanded Abstracts.
- 542 Krohn, D. A., T. MacDougall, and A. Mendez, 2000, Fiber optic sensors: fundamentals and appli-
543 cations: Isa.
- 544 Lindsey, N. J., E. R. Martin, D. S. Dreger, B. Freifeld, S. Cole, S. R. James, B. L. Biondi, and J. B.
545 Ajo-Franklin, 2017, Fiber-optic network observations of earthquake wavefields: Geophysical
546 Research Letters.
- 547 Mateeva, A., J. Lopez, J. Mestayer, P. Wills, B. Cox, D. Kiyashchenko, Z. Yang, W. Berlang, R.
548 Detomo, and S. Grandi, 2013, Distributed acoustic sensing for reservoir monitoring with vsp:
549 The Leading Edge, **32**, 1278–1283.
- 550 Mateeva, A., J. Lopez, H. Potters, J. Mestayer, B. Cox, D. Kiyashchenko, P. Wills, S. Grandi, K.
551 Hornman, B. Kuvshinov, et al., 2014, Distributed acoustic sensing for reservoir monitoring with
552 vertical seismic profiling: Geophysical Prospecting, **62**, 679–692.
- 553 Matzel, E., X. Zeng, C. Thurber, Y. Luo, C. Morency, et al., 2017a, Seismic interferometry using

554 the dense array at the brady geothermal field.

555 Matzel, E. M., X. Zeng, C. Thurber, and C. Morency, 2017b, Using Virtual Earthquakes to Charac-

556 terize the Material Properties of the Brady Hot Springs , Nevada: Geothermal Resources Council.

557 Mestayer, J., B. Cox, P. Wills, D. Kiyashchenko, J. Lopez, M. Costello, S. Bourne, G. Ugueto,

558 R. Lupton, G. Solano, et al., 2011, Field trials of distributed acoustic sensing for geophysical

559 monitoring, *in* SEG Technical Program Expanded Abstracts 2011: Society of Exploration Geo-

560 physicists, 4253–4257.

561 Parker, T., S. Shatalin, and M. Farhadiroushan, 2014, Distributed Acoustic Sensing - A new tool for

562 seismic applications: First Break, **32**, 61–69.

563 Rocha, D., N. Tanushev, and P. Sava, 2016, Isotropic elastic wavefield imaging using the energy

564 norm: Geophysics, **81**, S207–S219.

565 Russakovsky, O., J. Deng, H. Su, J. Krause, S. Satheesh, S. Ma, Z. Huang, A. Karpathy, A. Khosla,

566 M. Bernstein, A. C. Berg, and L. Fei-Fei, 2015, ImageNet Large Scale Visual Recognition Chal-

567 lenge: International Journal of Computer Vision (IJCV), **115**, 211–252.

568 Samuel, A. L., 1959, Some studies in machine learning using the game of checkers: IBM Journal

569 of research and development, **3**, 210–229.

570 Siler, D. L., and J. E. Faulds, 2013, Three-dimensional geothermal fairway mapping: Examples

571 from the western great basin, usa,: GRC Transactions, **7**, 327–332.

572 Szegedy, C., V. Vanhoucke, S. Ioffe, J. Shlens, and Z. Wojna, 2015, Rethinking the Inception Ar-

573 chitecture for Computer Vision.

574 Trainor-Guitton, W. J., A. Ramirez, X. Yang, K. Mansoor, Y. Sun, and S. Carroll, 2013, Value

575 of information methodology for assessing the ability of electrical resistivity to detect co2/brine

576 leakage into a shallow aquifer: International Journal of Greenhouse Gas Control, **18**, 101–113.

LIST OF FIGURES

577 1 PoroTomo survey geometry. Green dots represent source locations, red dots represent geo-

578 phone locations, and the blue line represents the surface DAS layout.

579 2 Consider a source that generates both P and S waves; this is a 2D Homogeneous, flat-

580 layered, isotropic ray path example. The blue lines represent ray paths of the labeled waves, the

581 blue arrow represents the propagation direction of the wave, the green line represents a horizontal

582 reflector in the subsurface, and the yellow star represents the source. (a) Demonstration of P-P wave

583 effect on the fiber using ray paths. Particle motion is inline with propagation direction (blue arrow).

584 The fiber will only record data at large offsets. (b) Demonstration of SV-SV wave effect on the fiber

585 using ray paths. Particle motion is perpendicular with the propagation direction (green arrows). The

586 fiber will only record data at short offsets.

587 3 Amplitude versus emerging angle for both geophone (blue) and horizontal DAS (red). An

588 emerging angle of 0° indicates a wave that is propagating perpendicular to the surface and an emerg-

589 ing angle of 90° degrees indicated a wave is propagating parallel to the surface. (a) Sensitivity with

590 respect to a P-wave at different emerging angles of horizontal DAS (red) and geophone z-component

591 (blue). (b) Sensitivity with respect to an SV-wave at different emerging angles of horizontal DAS

592 (red) and geophone x-component (blue).

593 4 Siler and Faulds (2013) fault density mapping within the PoroTomo Survey box. This

594 model was used as a reflectivity model for the experiments within this section.

595 5 Reflectivity model from Siler and Faulds (2013) extracted at the location of Well 56-A1

596 used for simulating data. Blue dots represent source locations and the red dots represent geophone

597 locations. DAS fiber was placed between the geophone locations.

598 6 (a) Resulting image from migrating geophone synthetic data. (b) Resulting image from

599 migrating DAS synthetic data. (c) Combined image from migrating DAS and geophone synthetic

600 data.

601 7 (a) Resulting image from migrating geophone synthetic data. (b) Resulting image from
602 migrating DAS synthetic data. (c) Combined image from migrating DAS and geophone synthetic
603 data.

604 8 (a) Examples of the automatically generated faults images used to train the CNN. (b) Ex-
605 amples of the automatically generated images that were not faults used to train the CNN.

606 9 Posterior reliability of information from CNN's calculated using Equation 3 using (a) a
607 vertical force and (b) a horizontal force. The objective is to maximize the percentages of true posi-
608 tives and negatives (green arrows) while minimizing the percentages of false positives and negatives
609 (red arrows). This is obtained by having better instruments as well as better classification.

610 10 Body wave (P-wave) velocity (m/s) model from sweep interferometry in 3D perspective
611 (Matzel et al., 2017b).

612 11 Four layer model with a variety of structures used for data modeling. This model is used
613 as a density model for elastic modeling.

614 12 Results of migrating the reflectivity model (Figure 11) using the PoroTomo DAS acquisi-
615 tion shown on the right. The true reflectivity model is overlain and shown on the left. The slices on
616 each side are taken at the yellow cross shown on the map view of the acquisition.

617 13 Results of migrating the reflectivity model (Figure 11) using the PoroTomo geophone ac-
618 quisition shown on the right. The true reflectivity model is overlain and shown on the left. The
619 slices on each side are taken at the yellow cross shown on the map view of the acquisition.

620 14 Posterior reliability of information from energy norm filtering calculated using Equation 3
621 using a horizontal force. The objective is to maximize the percentages of true positives and nega-
622 tives (green arrows) while minimizing the percentages of false positives and negatives (red arrows).

623 15 New survey geometry proposed to test the effectiveness of surface DAS fiber. Green dots

624 represent source locations, red dots represent geophone locations, and the blue lines represent the
625 surface DAS acquisition.

626 16 Posterior reliability of information using a horizontal force and the Figure 15 acquisition
627 geometry.

628

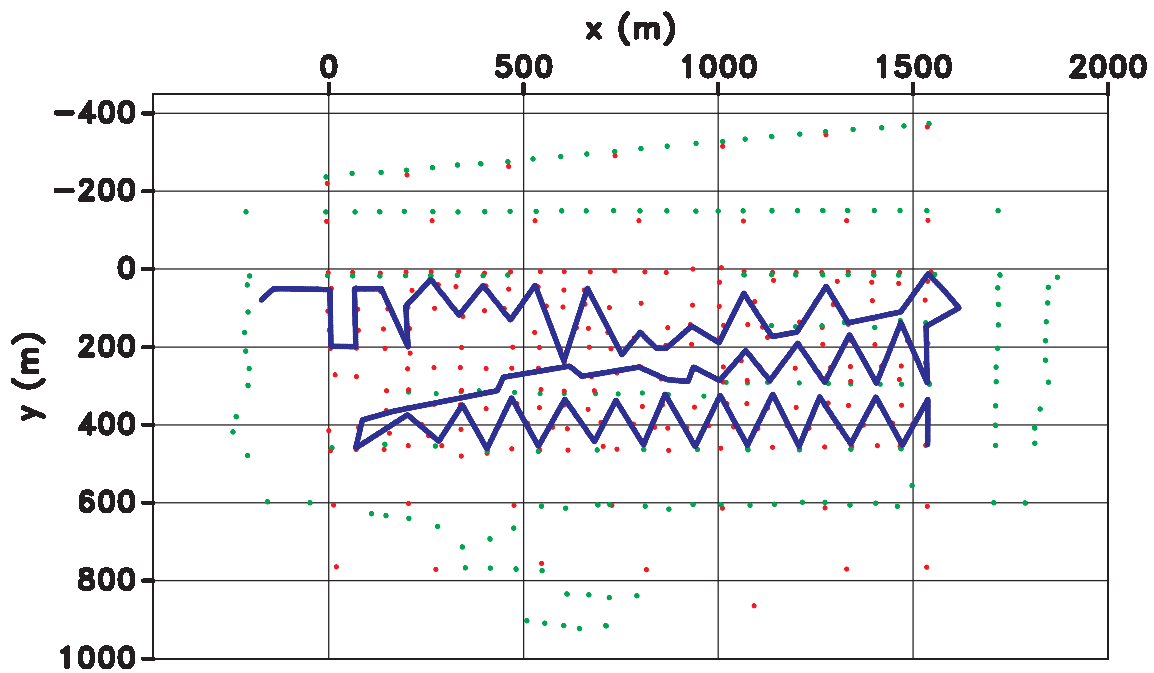
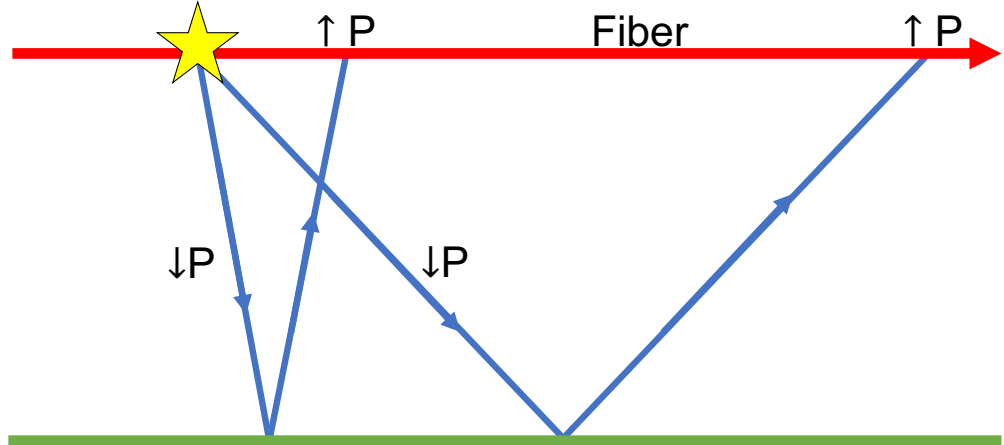
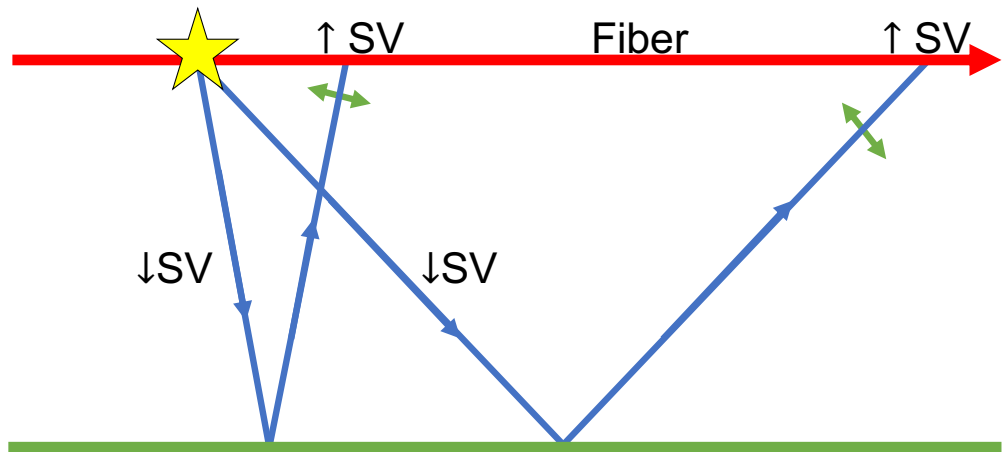


Figure 1: PoroTomo survey geometry. Green dots represent source locations, red dots represent geophone locations, and the blue line represents the surface DAS layout.



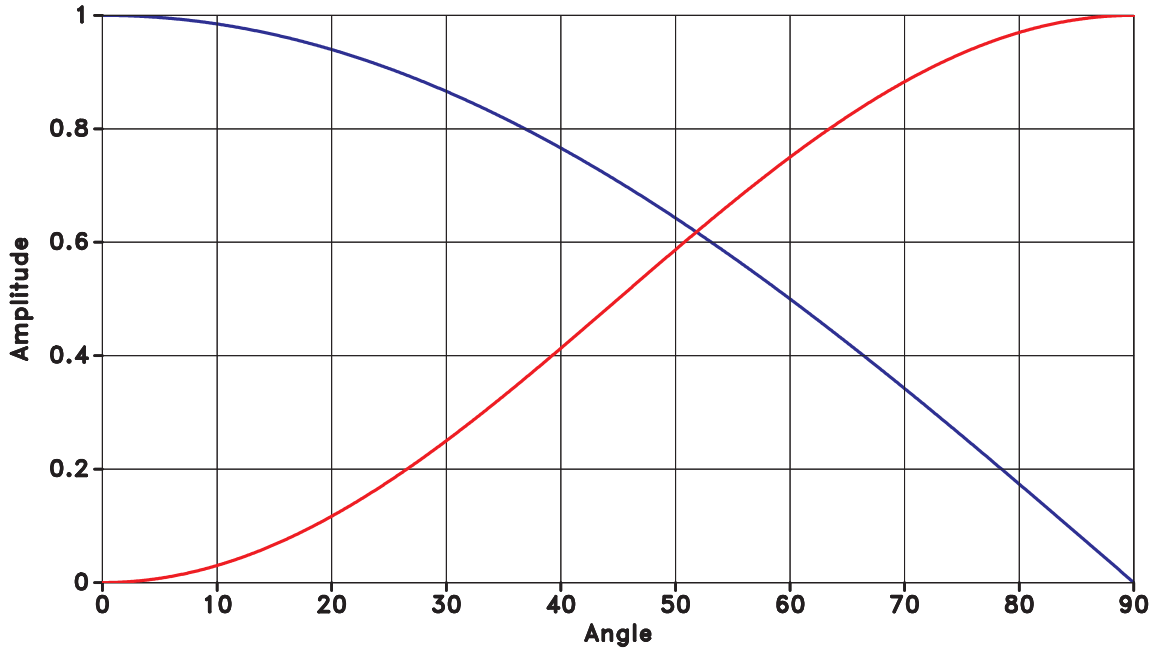
(a)



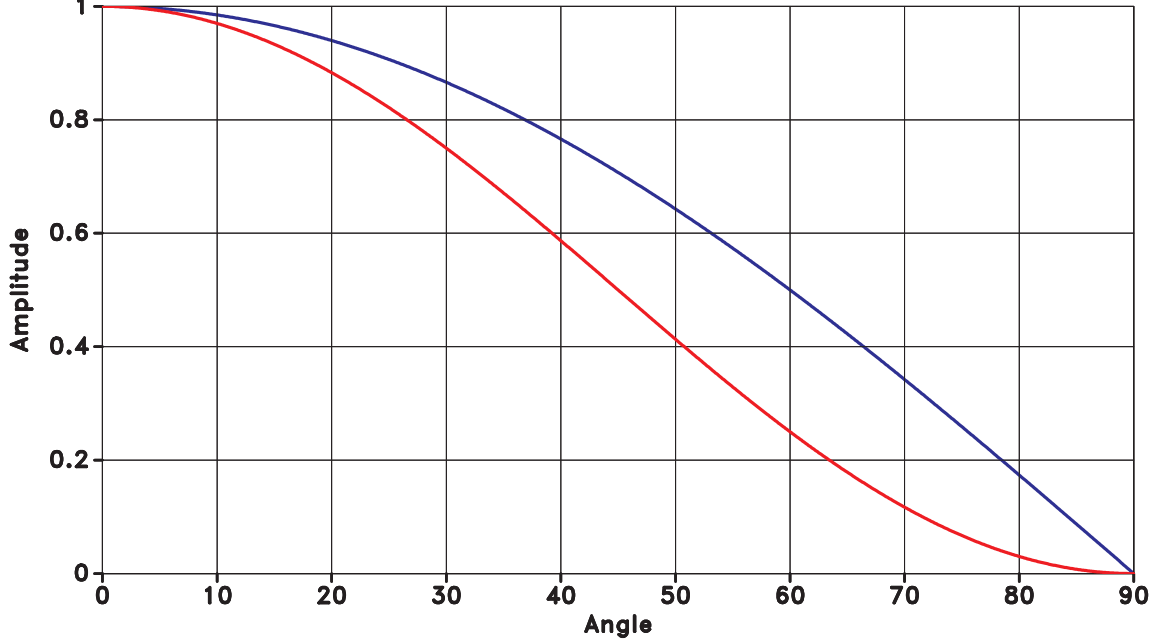
(b)

Figure 2: Consider a source that generates both P and S waves; this is a 2D Homogeneous, flat-layered, isotropic ray path example. The blue lines represent ray paths of the labeled waves, the blue arrow represents the propagation direction of the wave, the green line represents a horizontal reflector in the subsurface, and the yellow star represents the source. (a) Demonstration of P-P wave effect on the fiber using ray paths. Particle motion is inline with propagation direction (blue arrow). The fiber will only record data at large offsets. (b) Demonstration of SV-SV wave effect on the fiber using ray paths. Particle motion is perpendicular with the propagation direction (green arrows). The fiber will only record data at short offsets.

-



(a)



(b)

Figure 3: Amplitude versus emerging angle for both geophone (blue) and horizontal DAS (red). An emerging angle of 0° indicates a wave that is propagating perpendicular to the surface and an emerging angle of 90° degrees indicated a wave is propagating parallel to the surface. (a) Sensitivity with respect to a P-wave at different emerging angles of horizontal DAS (red) and geophone z-component (blue). (b) Sensitivity with respect to an SV-wave at different emerging angles of horizontal DAS (red) and geophone x-component (blue).

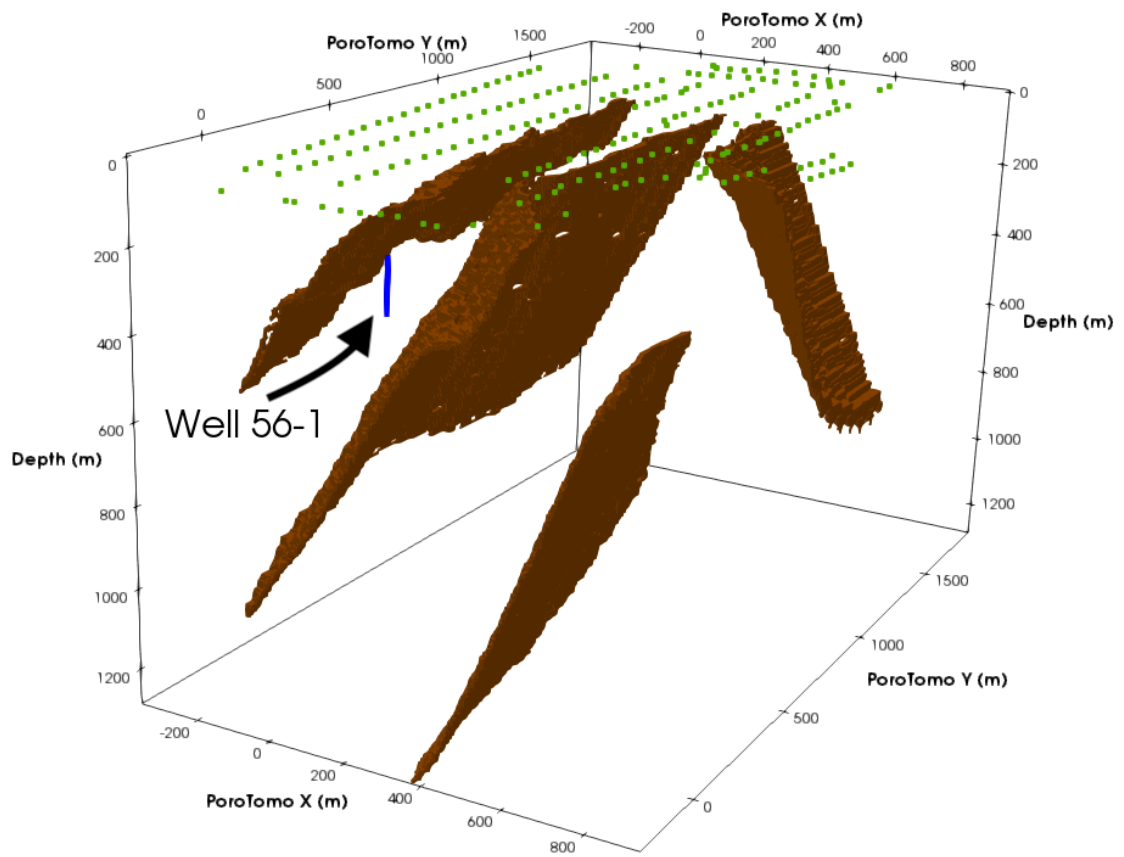


Figure 4: Siler and Faulds (2013) fault density mapping within the PoroTomo Survey box. This model was used as a reflectivity model for the experiments within this section.

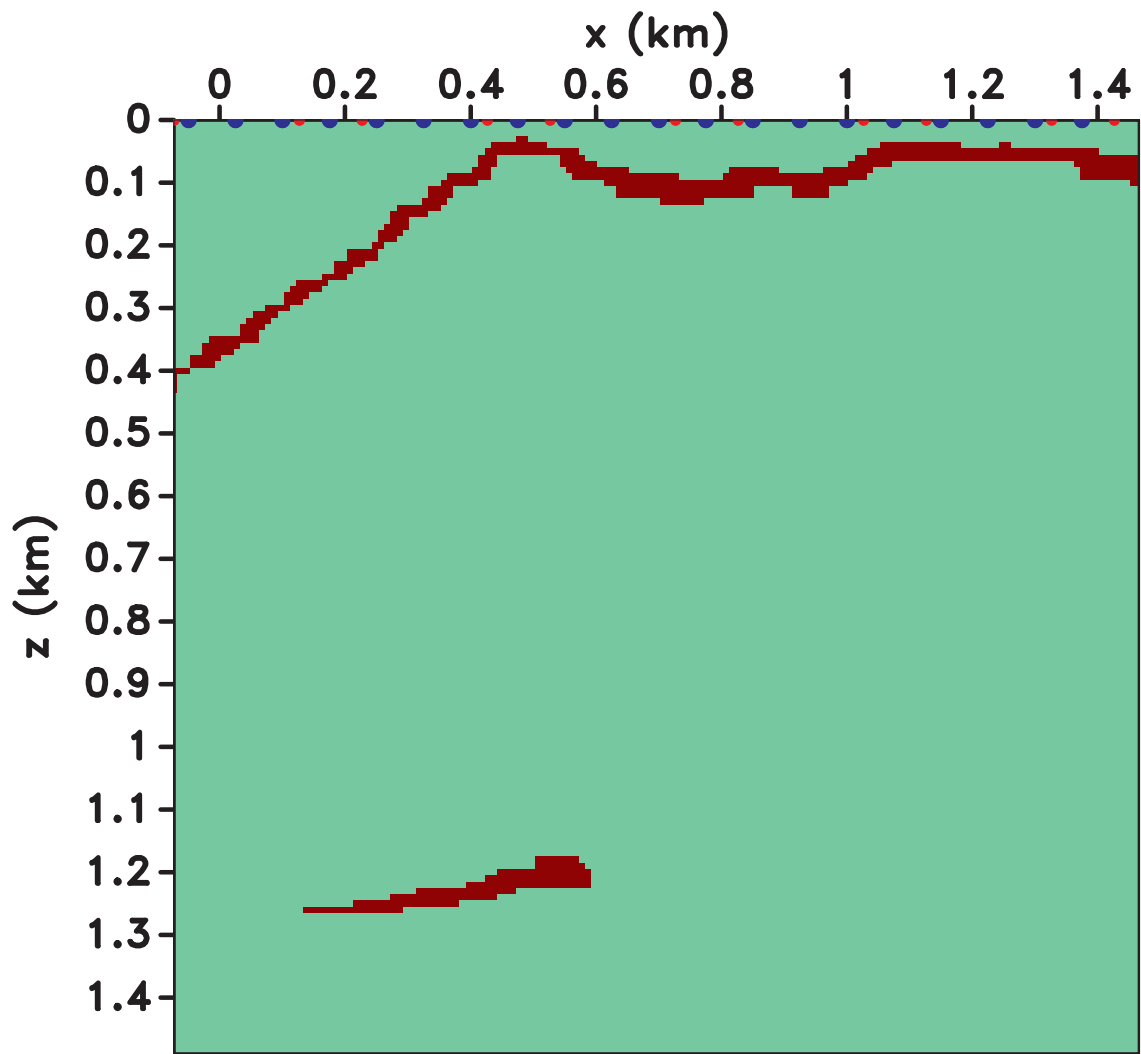


Figure 5: Reflectivity model from Siler and Faulds (2013) extracted at the location of Well 56-A1 used for simulating data. Blue dots represent source locations and the red dots represent geophone locations. DAS fiber was placed between the geophone locations.

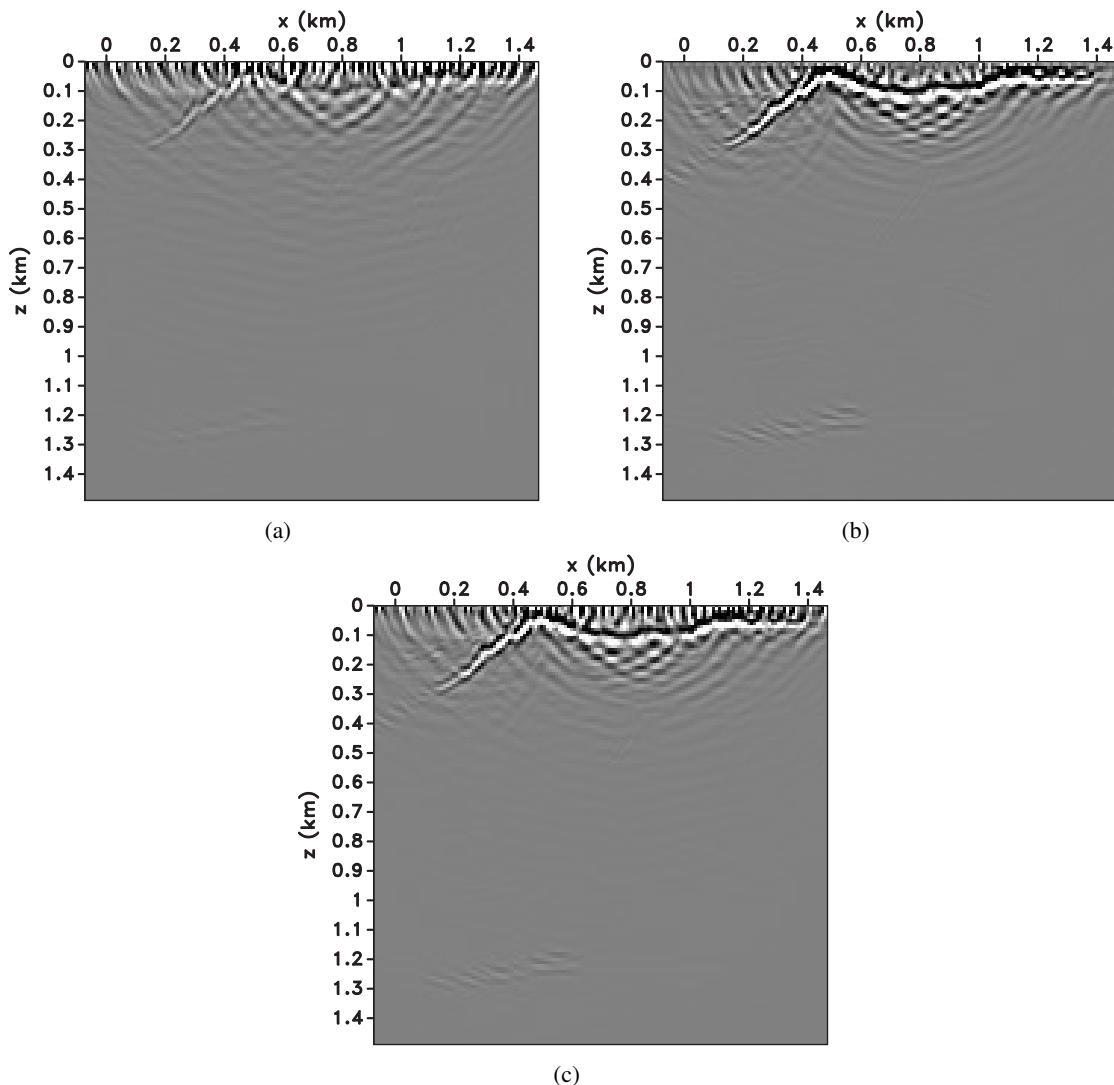


Figure 6: (a) Resulting image from migrating geophone synthetic data. (b) Resulting image from migrating DAS synthetic data. (c) Combined image from migrating DAS and geophone synthetic data.

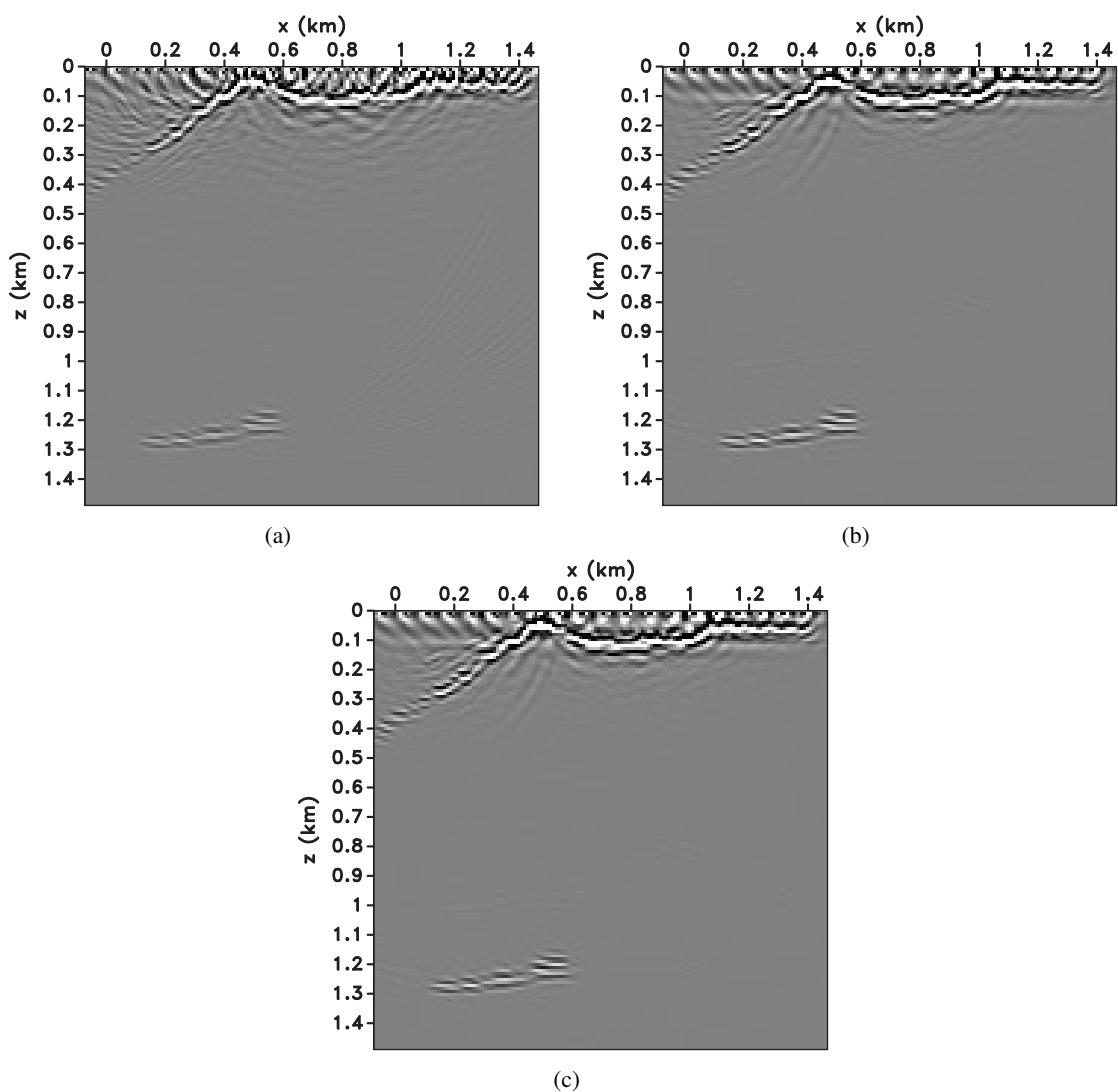


Figure 7: (a) Resulting image from migrating geophone synthetic data. (b) Resulting image from migrating DAS synthetic data. (c) Combined image from migrating DAS and geophone synthetic data.

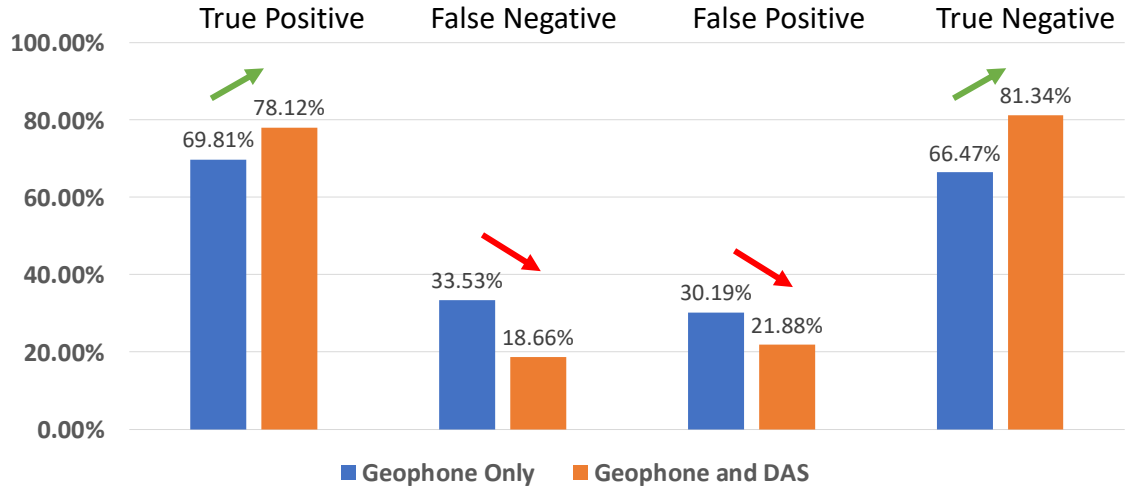


(a)

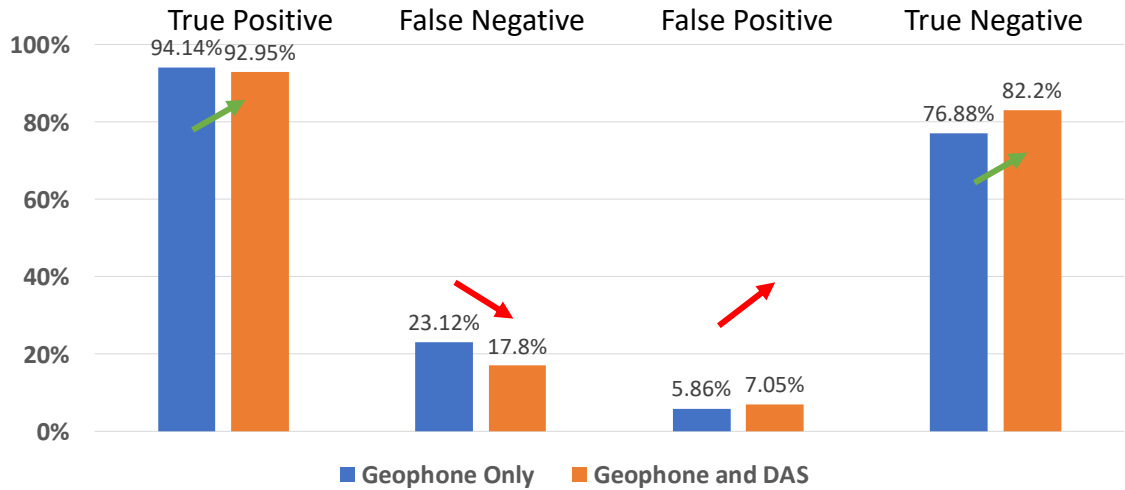


(b)

Figure 8: (a) Examples of the automatically generated faults images used to train the CNN. (b) Examples of the automatically generated images that were not faults used to train the CNN.



(a)



(b)

Figure 9: Posterior reliability of information from CNN's calculated using Equation 3 using (a) a vertical force and (b) a horizontal force. The objective is to maximize the percentages of true positives and negatives (green arrows) while minimizing the percentages of false positives and negatives (red arrows). This is obtained by having better instruments as well as better classification.

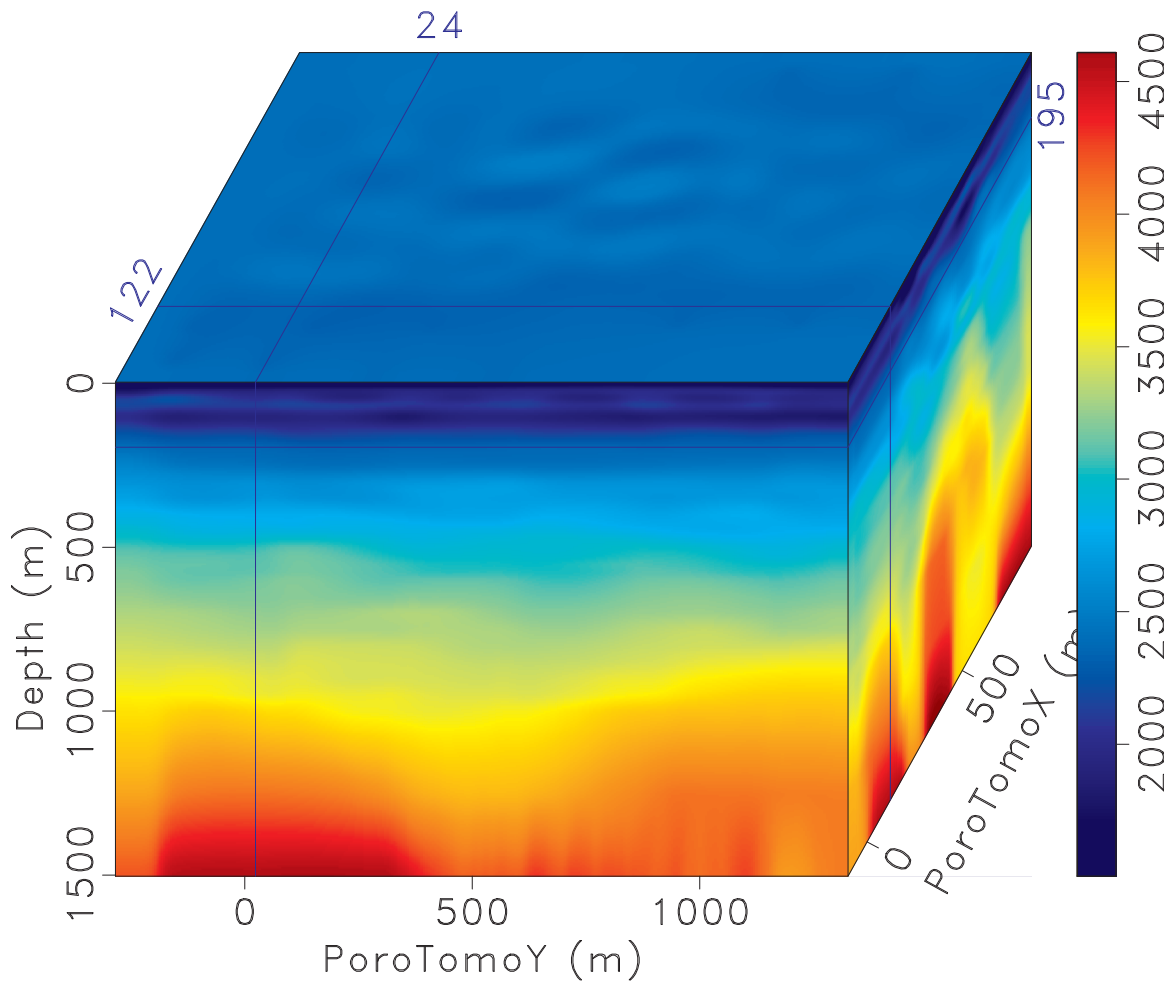


Figure 10: Body wave (P-wave) velocity (m/s) model from sweep interferometry in 3D perspective (Matzel et al., 2017b).

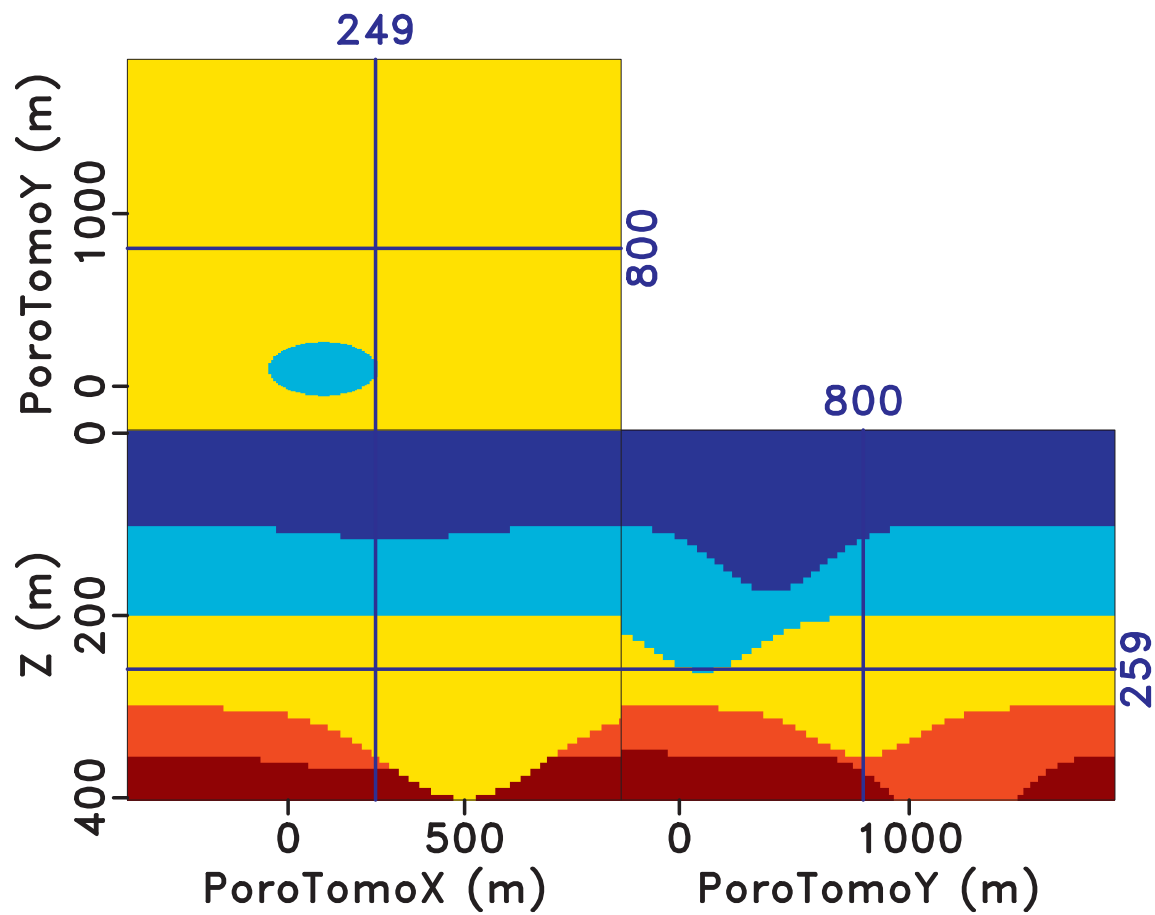


Figure 11: Four layer model with a variety of structures used for data modeling. This model is used as a density model for elastic modeling.

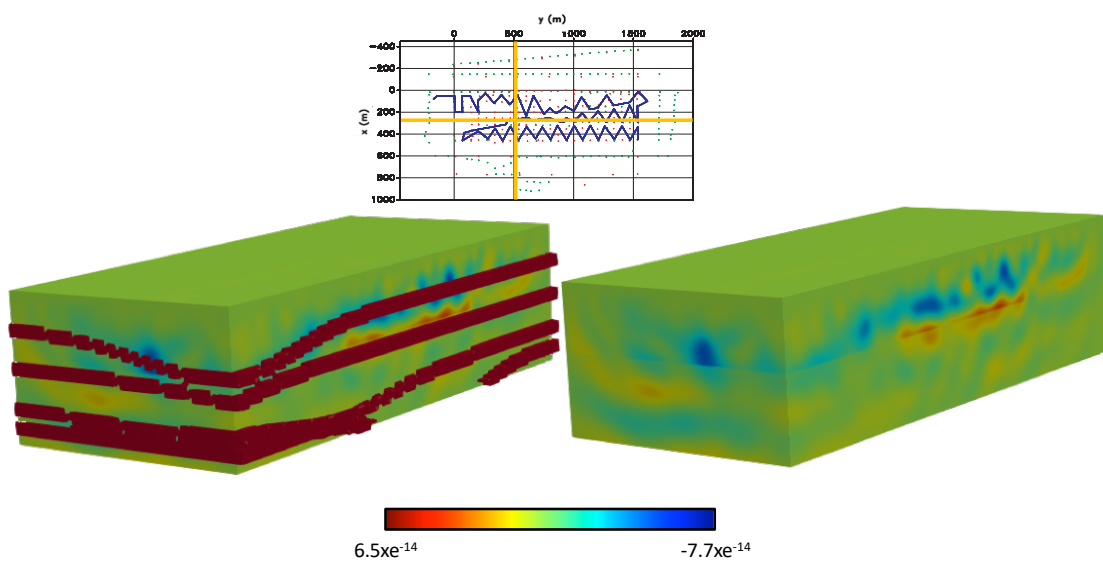


Figure 12: Results of migrating the reflectivity model (Figure 11) using the PoroTomo DAS acquisition shown on the right. The true reflectivity model is overlain and shown on the left. The slices on each side are taken at the yellow cross shown on the map view of the acquisition.

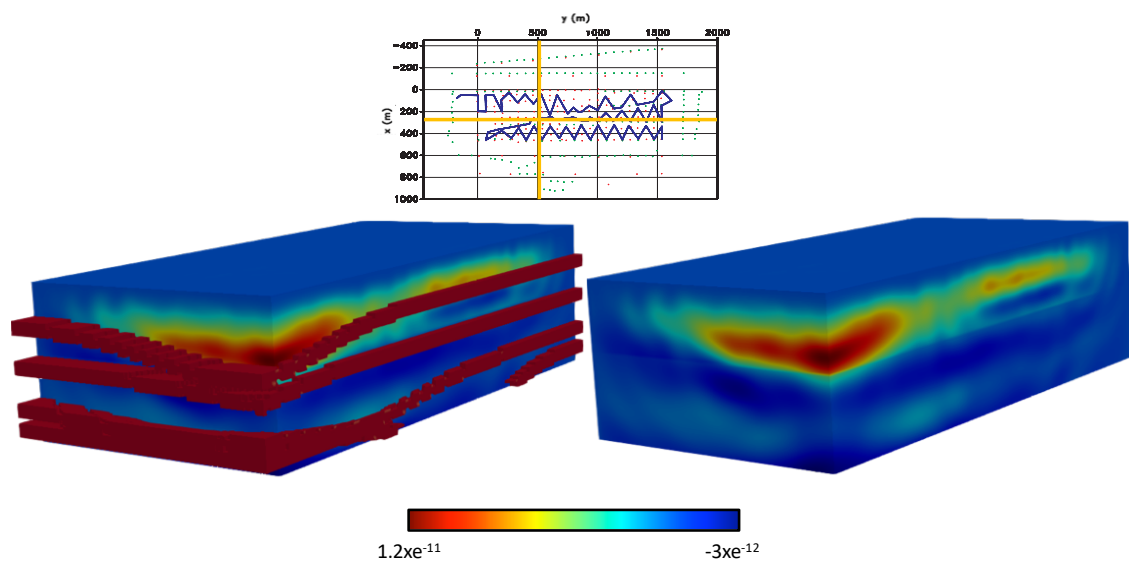


Figure 13: Results of migrating the reflectivity model (Figure 11) using the PoroTomo geophone acquisition shown on the right. The true reflectivity model is overlain and shown on the left. The slices on each side are taken at the yellow cross shown on the map view of the acquisition.

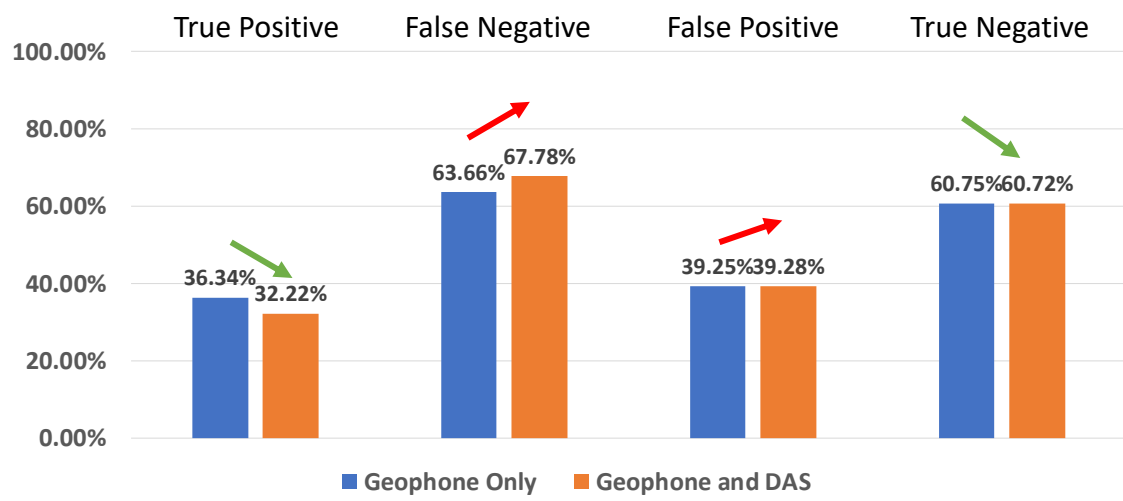


Figure 14: Posterior reliability of information from energy norm filtering calculated using Equation 3 using a horizontal force. The objective is to maximize the percentages of true positives and negatives (green arrows) while minimizing the percentages of false positives and negatives (red arrows).

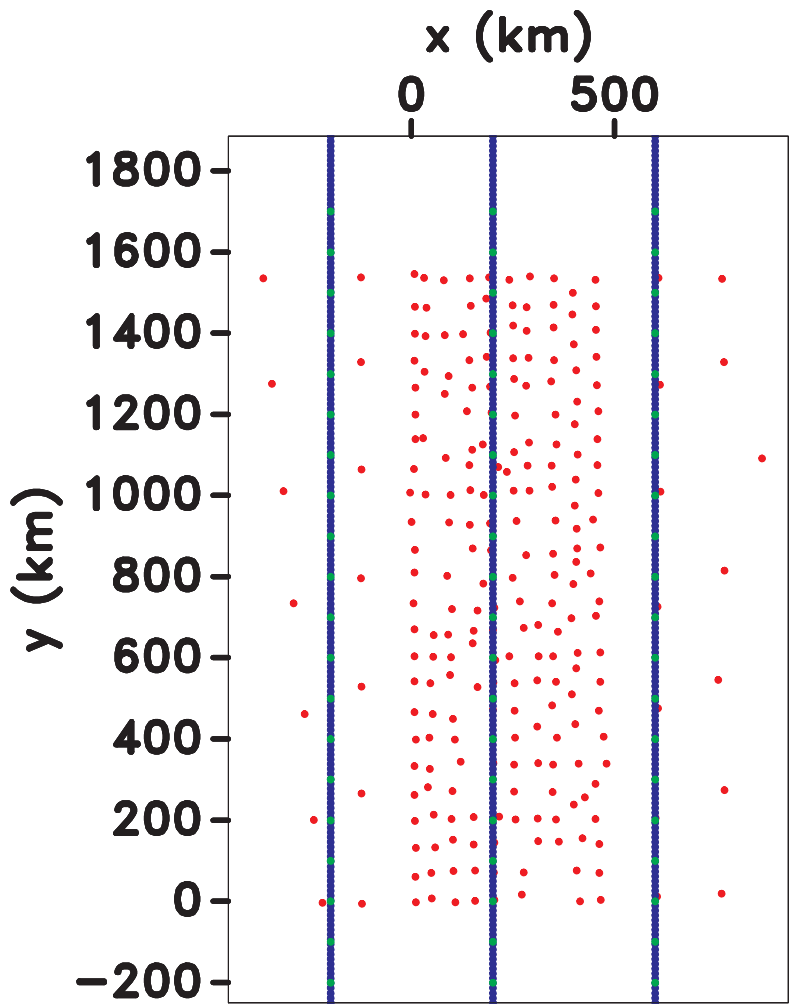


Figure 15: New survey geometry proposed to test the effectiveness of surface DAS fiber. Green dots represent source locations, red dots represent geophone locations, and the blue lines represent the surface DAS acquisition.

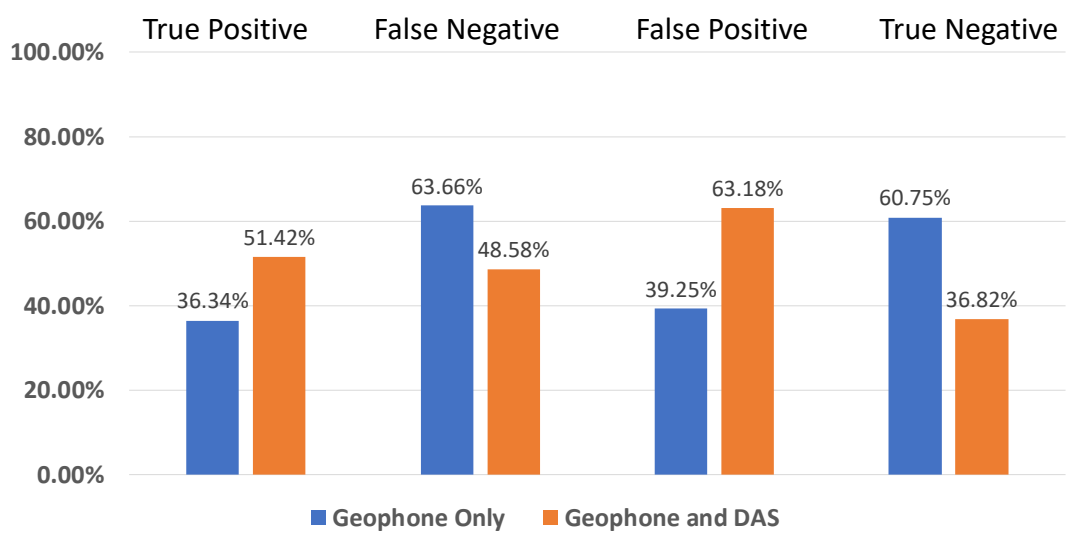


Figure 16: Posterior reliability of information using a horizontal force and the Figure 15 acquisition geometry.